

# Correlation and Non-Orthogonality Figures of Merit of Beamforming Fields

Reza Gheybi Zarnagh\*, Andrés Alayón Glazunov\*

\*Department of Electrical Engineering, University of Twente, Enschede, The Netherlands

\*{r.gheybizarnagh; a.alayonglazunov}@utwente.nl

**Abstract**—New figures of merit are introduced to characterize the correlation and the non-orthogonality of multiple beams produced by an array antenna or two different array antennas. The figures of merit take into account the correlation or non-orthogonality between beamforming fields of two separate arrays and the beams produced by each at once. As an example, two adjacent modified microstrip Franklin array antennas have been designed. The non-orthogonality and isolation between steered radiation patterns have been studied for arrays operating at the same center frequencies 77 GHz. Each array antenna consists of 5 linear sub-arrays with 10 rectangular microstrip patch elements. Chebyshev tapering and open circuit stubs have been applied to the microstrip patches to obtain a low side lobe level and better impedance matching between single elements, respectively. The achieved peak gain, minimum side lobe level (SLL) and impedance bandwidth are 14.1 dBi, −13.6 dB and 581 MHz for a single sub-array at 77 GHz, respectively. The evaluation has shown that the same pair of arrays have different non-orthogonality depending on the propagation channel. On the one hand, the evaluated array-pair shows highly uncorrelated performance in a rich isotropic multipath propagation environment. On the other hand, they show high non-orthogonality (or co-directionality) in a pure line-of-sight channel as expected. Hence, depending on the propagation channel, the arrays can be used for different communication and sensing applications either jointly or independently.

**Index Terms**—Joint Communications and Sensing, Beamforming Patterns, Isolation, Correlation Coefficient.

## I. INTRODUCTION

The fifth generation (5G) and beyond wireless systems foresee the emergence of many new applications. A hot research topic is the development of radar systems for increased safety of vehicles on the road. Also the potential realization of joint radar and communication systems is of great interest. Millimeter wave (mmWave) frequency bands might be utilized to produce high throughput communication systems due to the wide bandwidths available at mmWaves and the same hardware platforms and spectrum sharing. However, there exist radars operating at the 77 GHz since a few years already. There is a common interest to explore these bands for communication and sensing at the same frequency bands (full-duplex) which may lead to radio spectrum congestion [1]. Moreover, different frequencies are used for millimeter-wave (mm-wave) bands applications using the jointly designed structures and shared radiation apertures [2], [3]. In existing literature, one of the major problems in joint communication and sensing systems is the coupling of transmitting (TX) antenna and receiving (RX) antenna signal paths as well as the potential interference

between radar and communication radiation patterns of the antennas. In [4], sub-wavelength passive periodic structures realized as square mushroom are used between the Tx and Rx antennas to create high isolation at 26 GHz. The isolation between the Tx and Rx paths has been evaluated by simulating various insertion loss values showing that a good isolation of 50 dB can be achieved. However, there is a need to understand the behavior of beamforming patterns in the far-field when two array antennas are operating at the same frequency. The performance of different linear patch antenna array architectures in terms of self-interference cancellation performance and obtained maximum gain in the beam steering range has been evaluated [5]. The proposed arrays are designed to operate with the implementation of a self-interference cancellation algorithm required for true in-band full-duplex JCAS operation at the same frequency band.

The correlation and non-orthogonality of radiation patterns has been vastly studied, see e.g. [6], [7]. For multipath environments, the correlation coefficient between the antennas is often evaluated. A common figure of merit is the envelope correlation coefficient (ECC) which is a measure of the signal correlation in a rich isotropic multipath (RIMP) environment

$$\rho_{\text{ECC}} = \frac{|\oint \mathbf{F}_1 \cdot \mathbf{F}_2^* d\Omega|^2}{\oint |\mathbf{F}_1|^2 d\Omega \oint |\mathbf{F}_2|^2 d\Omega}, \quad (1)$$

where  $\mathbf{F}_1$  and  $\mathbf{F}_2$  are the embedded radiation patterns of the considered antennas and the symbol  $*$  denotes the complex conjugate operation. The symbol  $\cdot$  denotes the scalar product of two vectorial magnitudes. It is worthwhile to note that the integration is performed over the sphere of unit radius. The relation to RIMP becomes apparent because all directions are equiprobable. It is straightforward to see that the denominator is equal to  $16\pi^2$  for lossless perfectly matched antennas. On the other hand, in a pure line-of-sight (LOS) or equivalently in a Random LOS (RLOS or RanLOS), instead of the correlation the polarization non-orthogonality (or co-linearity) is evaluated [8]

$$\rho_{\text{NOR}} = \frac{|\mathbf{F}_1 \cdot \mathbf{F}_2^*|}{|\mathbf{F}_1| |\mathbf{F}_2|}, \quad (2)$$

where as above  $\mathbf{F}_1$  and  $\mathbf{F}_2$  are the embedded radiation patterns of the considered antennas. Clearly, if the antennas are orthogonally polarized it immediately follows that  $\rho_{\text{ECC}} = \rho_{\text{NOR}} = 0$ . On the other hand, if the radiation patterns are the same then  $\rho_{\text{ECC}} = \rho_{\text{NOR}} = 1$ . For all other conditions, partial

correlation or partial non-orthogonality will be observed and hence, the corresponding values will be greater than 0, but less than 1. Another important observation is that for sufficiently separated antennas the correlation between any two antennas in RIMP can also be 0 [6]. Furthermore, (1) is a single number because of the integration, while (2) is a function of both  $\theta$  and  $\phi$  because  $\mathbf{F}_1$  and  $\mathbf{F}_2$  depend on the direction of observation.

In the case of multiple-beam antennas or scanned-beam antennas the radiation pattern will change depending on the direction of observation. Moreover, depending on the scanning capability or the directions toward which the beams of the multi-beam antennas are directed, the correlation and the non-orthogonality may change. This has not been analyzed before and we aim at filling this gap in the present paper.

## II. BEAMFORMING FIELDS FIGURES OF MERIT

Here we introduce a generalization of the envelope correlation coefficient (1) and the polarization non-orthogonality (2) to the case of multi-beam or scanning beam antennas.

### A. Beam Correlation

An array antenna usually produces beams at different scanning directions. Then, by analogy with (1) we introduce the beam correlation (BC) of an array antenna

$$\rho_{11,BC}(\alpha, \beta) = \frac{\left| \oint \mathbf{F}_1(\alpha) \cdot \mathbf{F}_1^*(\beta) d\Omega \right|^2}{\oint |\mathbf{F}_1(\alpha)|^2 d\Omega \oint |\mathbf{F}_1(\beta)|^2 d\Omega}, \quad (3)$$

where here  $\mathbf{F}_1(\alpha)$  is the beamforming field of an array antenna at scanning (beamforming) angle  $\alpha$  and  $\mathbf{F}_1(\beta)$  is the beamforming field of the same array antenna at scanning angle  $\beta$ . Clearly, beams sufficiently separated in the angular domain can result in a low correlation, while obviously the correlation is full, i.e.,  $\rho_{11,BC}(\alpha, \beta) = 1$  for  $\alpha = \beta$ . Similarly, we can define the same type of correlation for two co-located or two distributed array antennas as a function of the scanning angles of their beams

$$\rho_{12,BC}(\alpha, \beta) = \frac{\left| \oint \mathbf{F}_1(\alpha) \cdot \mathbf{F}_2^*(\beta) d\Omega \right|^2}{\oint |\mathbf{F}_1(\alpha)|^2 d\Omega \oint |\mathbf{F}_2(\beta)|^2 d\Omega}, \quad (4)$$

where  $\mathbf{F}_1(\alpha)$  and  $\mathbf{F}_2(\beta)$  are the far-fields corresponding to two beamforming array antennas scanned in directions  $\alpha$  and  $\beta$ . We can interpret (3) as the beamforming-field directional auto-correlation, while (4) is the beamforming-field directional cross-correlation. Thus, the beamforming-field directional auto-correlation for array antenna 2 will be denoted by  $\rho_{11,BC}$ . It is straightforward to see that (4) becomes exactly zero if the beams of the two antennas are orthogonal in polarization, but as above for the single antennas, the correlation can be reduced if the arrays are separated in space or the produced beams are sufficiently separated in directions.

Depending on the application, it might be required that the two arrays generate highly correlated beams while scanning in the same direction, i.e.,  $\rho_{12,BC}(\alpha, \beta) = 1$  when  $\alpha = \beta$  and 0 in all other directions. The condition applies in this case for each of the array antennas, i.e.,  $\rho_{11,BC}(\alpha, \beta) = \rho_{22,BC}(\alpha, \beta) = 1$  and 0 in all other directions. In this case, a useful measure

of the overall correlation between the two antennas can be characterized by the product

$$\rho_{12,BCW}(\alpha, \beta) = \sqrt{\rho_{12,BC} \rho_{11,BC} \rho_{22,BC}}, \quad (5)$$

where  $\rho_{12,BC}$ ,  $\rho_{11,BC}$  and  $\rho_{22,BC}$  are given by the equations above and all depend on  $\alpha$  and  $\beta$ , which have been omitted for compactness. When the two array antennas have identical performance then  $\rho_{12,BCW} = \rho_{11,BC} = \rho_{22,BC}$ . The advantage of (5) is that it condenses the correlation between the beams of the two arrays antennas and the beams of the individual array antennas into one parameter.

### B. Beam Non-Orthogonality

Following a similar line of thought as above we here introduce, by analogy with (2), the beam non-orthogonality (BNO) of an array antenna

$$\rho_{11,BNO}(\alpha, \beta) = \frac{|\mathbf{F}_1(\alpha) \cdot \mathbf{F}_1^*(\beta)|}{|\mathbf{F}_1(\alpha)| |\mathbf{F}_1(\beta)|}, \quad (6)$$

where here  $\mathbf{F}_1(\alpha)$  is the beamforming field of an array antenna at scanning (beamforming) angle  $\alpha$  and  $\mathbf{F}_1(\beta)$  is the beamforming field of the same array antenna at scanning angle  $\beta$  as defined above. Also here we can introduce the beam non-orthogonality for two co-located or two distributed array antennas as a function of the scanning angles of their beams

$$\rho_{12,BNO}(\alpha, \beta) = \frac{|\mathbf{F}_1(\alpha) \cdot \mathbf{F}_2^*(\beta)|}{|\mathbf{F}_1(\alpha)| |\mathbf{F}_2(\beta)|}, \quad (7)$$

where, as above,  $\mathbf{F}_1(\alpha)$  and  $\mathbf{F}_2(\beta)$  are the far-fields corresponding to two beamforming array antennas scanned in directions  $\alpha$  and  $\beta$ . Hence, a condensed parameter follows from the above definitions

$$\rho_{12,BNOW}(\alpha, \beta) = \sqrt{\rho_{12,BNO} \rho_{11,BNO} \rho_{22,BNO}}, \quad (8)$$

where  $\rho_{12,BNO}$ ,  $\rho_{11,BNO}$  and  $\rho_{22,BNO}$  have been defined above and all depend on  $\alpha$  and  $\beta$ , which have been omitted for compactness. Following a symmetric analysis as above, we can clearly see that when both array antennas have identical performance then  $\rho_{12,BNOW} = \rho_{11,BNO} = \rho_{22,BNO}$ . The advantage of (8), as in the case of (5), relies on the fact that it condenses the non-orthogonality between the beams of the two arrays antennas and the beams of the individual array antennas into one parameter.

## III. DESIGN OF FRANKLIN ARRAY ANTENNAS

This section describes the design process and simulation results of a  $1 \times 10$  linear Franklin sub-array antenna and two adjacent  $5 \times 10$  linear arrays comprising each 5 elements. Both arrays have been jointly designed on the same PCB. The designed array antennas are simulated and optimized with the CST Microwave Studio simulation software. They are used here for purpose of illustrating the correlation and non-orthogonality figures of merit introduced above on the basis of realistic antennas.

TABLE I  
ANTENNA DESIGN MEASURES.

$AEI(n)$	1&10	2&9	3&8	4&7	5&6
$L_{pn}(mm)$	1.12	1.12	1.12	1.12	1.12
$W_{pn}(mm)$	0.508	0.724	1	1.24	1.54
$L_{gn}(mm)$	0.935	0.982	1.67	1.28	1.34
$W_{gn}(mm)$	0.18	0.11	0.142	0.11	0.12
$L_s(mm)$	0.398	0.398	0.398	0.398	0.398
$W_s(mm)$	0.2	0.2	0.2	0.2	0.2
Parameter	$L_u$	$W_u$	$L_l$	$L_g$	$W_g$
Value(mm)	29.4	5.5	0.924	0.34	0.1

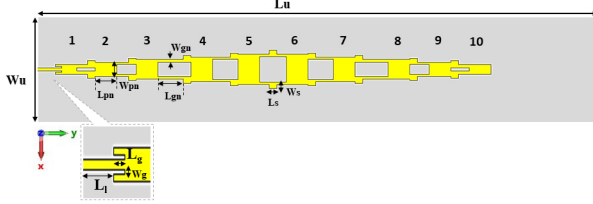


Fig. 1. The  $1 \times 10$  Chebyshev tapered rectangular Franklin array antenna configuration and corresponding element numbers.

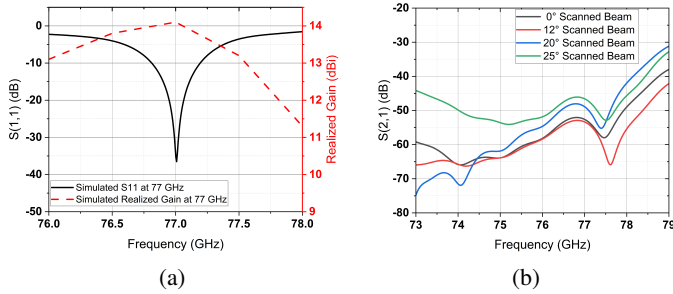


Fig. 2. (a) Simulated Reflection coefficient and realized gain for the Franklin sub-array at 77 GHz, and (b) comparison of simulated insertion loss results of array antennas at different center to center distances and scanning angles.

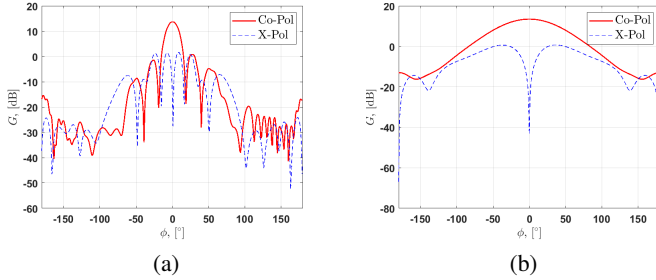


Fig. 3. Co-polarized and X-polarized simulated patterns of the  $1 \times 10$  Franklin sub-array at 77 GHz (a) E-plane and (b) H-plane.

#### A. The $1 \times 10$ Sub-Array Antenna

A microstrip linear Franklin array with 10 rectangular elements is designed to operate at 77 GHz. The configuration of the designed linear sub-array is illustrated in Fig. 1. The dimensions of the elements are given in Table I. The linear sub-array is designed on the Rogers RT5880 substrate with a thickness of 0.252 mm,  $\epsilon_r = 2.2$  and  $\tan\sigma = 0.0009$ . The linear sub-array is comprised of 10 rectangular single

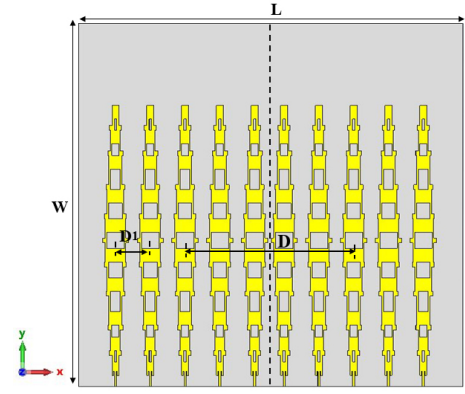


Fig. 4. Geometry of the simulated  $5 \times 10$  array antenna based on Franklin sub-arrays.

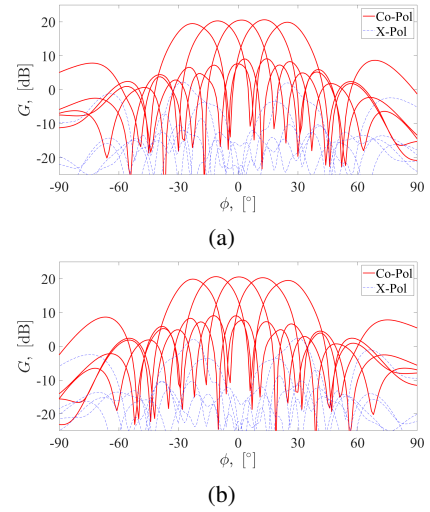


Fig. 5. Co-polarized and X-polarized simulated scanned patterns (E-plane) at 77 GHz of the  $5 \times 10$  (a) left and (b) right array antennas.

microstrip patch elements which are fed by two series microstrip lines. An inset microstrip feed line at the input of the sub-array is used as the excitation for the whole linear sub-array. Symmetric open circuit stubs are used to achieve better impedance matching. Fig. 2(a) shows the return loss results demonstrating a good impedance matching at the input of antenna and between elements. Also, the simulated realized gain at azimuth angle ( $\phi = 0^\circ$ ) values for the 76 to 78 GHz frequency band is shown in Fig. 2(a). The Chebyshev tapering technique is applied to change the widths of each of the rectangular microstrip patches according to the Chebyshev coefficients values. The reduced side lobe level of 13.6 dB from the main beam gain is obtained at the operating frequency 77 GHz. The simulated E-plane ( $\phi = 0^\circ$ ) and H-plane ( $\phi = 90^\circ$ ) radiation patterns are shown in Fig. 3.

#### B. The $5 \times 10$ Array Antennas

Two  $5 \times 10$  array antennas located side by side were simulated. They may represent an example of arrays that can be used for either communication or sensing, or either as the

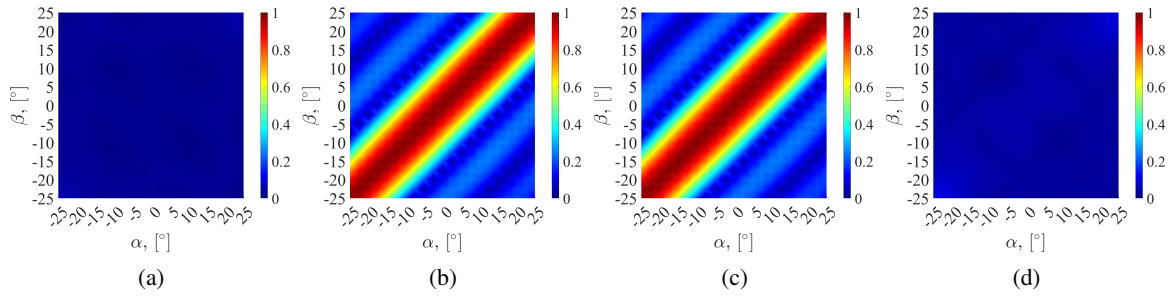


Fig. 6. Beam correlation between the 5 beams shown in Fig. 5 as a function of the scanning angles of the two simulated arrays. (a)  $\rho_{12,BC}$ , (b)  $\rho_{11,BC}$ , (c)  $\rho_{22,BC}$ , and (d)  $\rho_{12,BCW}$ .

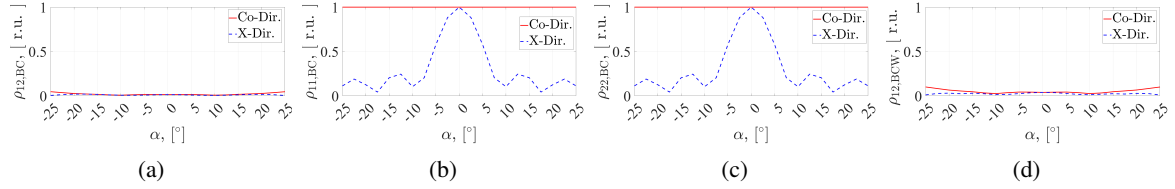


Fig. 7. Beam correlation between the 5 beams shown in Fig. 5 as a function of the scanning angle. Two cuts are taken from Fig. 6, along the diagonal denoted by Co-Dir., and along the anti-diagonal denoted by X-Dir. (a)  $\rho_{12,BC}$ , (b)  $\rho_{11,BC}$ , (c)  $\rho_{22,BC}$ , and (d)  $\rho_{12,BCW}$ .

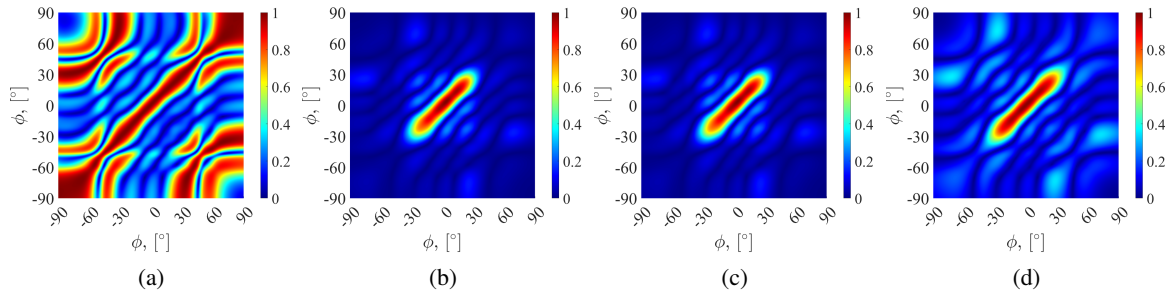


Fig. 8. Beam non-orthogonality for the 5 beams shown in Fig. 5 as a function of azimuth. All five beams are shown simultaneously. (a)  $\rho_{12,BNO}$ , (b)  $\rho_{11,BNO}$ , (c)  $\rho_{22,BNO}$ , and (d)  $\rho_{12,BNOW}$ .

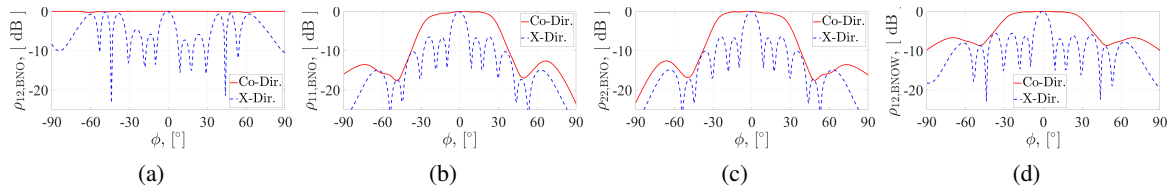


Fig. 9. Beam non-orthogonality for the 5 beams shown in Fig. 5 as a function of azimuth. All five beams are shown simultaneously. Two cuts are taken from Fig. 8, along the diagonal denoted by Co-Dir. and along the anti-diagonal denoted by X-Dir. (a)  $\rho_{12,BNO}$ , (b)  $\rho_{11,BNO}$ , (c)  $\rho_{22,BNO}$ , and (d)  $\rho_{12,BNOW}$ .

transmitter (Tx) and receiver (Rx) parts of a communication system or as the Tx and Rx parts of a radar system. The two adjacent arrays are shown in Fig. 4. The inter-element distances are chosen to be  $D_1 = 2.6$  mm, which is less than the wavelength of antennas in free space ( $< \lambda_0$ ) at the center operating frequency of 77 GHz. The center-to-center distance between the two arrays is  $D = 12.6$  mm. The overall dimensions for the arrays are  $(L = 28.7) \times (W = 30) \times 0.252$  mm<sup>3</sup>. Beamforming is computed for each array and the radiation patterns are scanned from  $\phi = -25^\circ$  to  $\phi = 25^\circ$  in the azimuth plane as shown in Fig. 5. Finally, the insertion loss results at

different scanning angles are illustrated in Fig. 2(b). As can be seen, the isolation is rather high at such close distances between the arrays.

#### IV. EVALUATION OF THE BEAM CORRELATION AND NON-ORTHOGONALITY

Fig. 6 shows the beam correlation between the 5 beams shown in Fig. 5 as a function of the scanning angles of the two simulated arrays. The subplots show (a)  $\rho_{12,BC}$ , (b)  $\rho_{11,BC}$ , (c)  $\rho_{22,BC}$ , and (d)  $\rho_{12,BCW}$ . As can be seen from Fig. 6(a) the two arrays produce beams that are fully uncorrelated for all the considered scanning angles. This means that in a RIMP

channel the received signals due to beams of the two adjacent channels are fully uncorrelated even if they point in the same direction. On the other hand, the received signals of beams from the same array are correlated mainly when pointing in the same directions, i.e., both beams coincide. However, as the beams are pointing in different directions the correlation rapidly decreases. The compound figure of merit shown in Fig. 6(d) the correlation will be stay low independently of the correlation of the individual array antennas. Hence, in this specific case the behaviour of each individual array does not have a mayor impact on the beam correlation.

Fig. 7 just reinforces the observations from above. Both arrays produce uncorrelated beams. And as expected beams from the same array become highly correlated (auto-correlated) when looking at close points in the angle-domain, in the other directions correlation drops after  $5^\circ$  or  $10^\circ$ , see Figs. 7(b) and (c). The compound effect shown in Fig. 7(d) is dominated by beamforming de-correlation between the two spatially separated array antennas.

Fig. 8 shows the beam non-orthogonality for the 5 beams shown in Fig. 5 as a function of azimuth angle. All five beams are shown simultaneously. The specific subplots show (a)  $\rho_{12,BNO}$ , (b)  $\rho_{11,BNO}$ , (c)  $\rho_{22,BNO}$ , and (d)  $\rho_{12,BNOW}$ . As can be seen from Fig. 8(a) there is a high beam non-orthogonality at different directions, but mostly in the direction where both arrays' beams are pointing in the same direction. Fig. 8(b) and (c) show that the beam non-orthogonality of both array antennas is confined to the main plane of radiation and within the field of view of the scanned beams (compare to Fig. 5). The compound figure of merit shown in Fig. 8(d) illustrates that even if the non-orthogonality is high in many direction of observation, the relevance is weighted by the behaviour of each individual array due to the limited field of view.

Fig. 9 is the beam non-orthogonality for the 5 beams shown in Fig. 5 as a function of azimuth. Two cuts are taken from Fig. 8, along the diagonal denoted by Co-Dir. and along the anti-diagonal denoted by X-Dir. All five beams are shown simultaneously. (a)  $\rho_{12,BNO}$ , (b)  $\rho_{11,BNO}$ , (c)  $\rho_{22,BNO}$ , and (d)  $\rho_{12,BNOW}$ . These plots are presented to further clarify the non-orthogonality of the beams of the two array antennas when they are pointing towards the same direction (Co-Dir.) and where they are pointing away from each other (X-Dir.). Clearly, as explained above the two arrays are non-orthogonal in the main direction of radiation of the beams.

## V. CONCLUSION

In this paper, we have presented new figures of merits to evaluate the correlation and the non-orthogonality resulting from beamforming fields from multi-beam and phased-array antennas. The workings of the figures of merit were shown on the example of array antennas based on a microstrip linear series-fed Franklin array antenna operating at the 77 GHz frequency band. The Chebyshev coefficients were applied to the microstrip patch antennas in order to decrease the side lobe level. Also, open-circuit stubs were symmetrically located at the input of each single element patch antenna to enhance

the impedance matching and better excitation of rectangular patches. A system comprising two adjacently positioned array antennas consisting of 5 Franklin sub-arrays were designed and evaluated in terms of the proposed figures of merit. Since, the isolation between two arrays is one of the major issues in designing systems for joint communication and sensing applications, the correlation and the non-orthogonality of the beamforming patterns by the array antennas in the far-field are important to evaluate. Our analysis show that the beamforming fields produced by the two arrays are uncorrelated in rich multipath environments, but have high correlation in pure- or random line-of-sight environments.

## ACKNOWLEDGMENT

This work has been funded by the H2020-MSCA Project 955629 ITN-5VC.

## REFERENCES

- [1] B. Paul, A. R. Chiriyath and D. W. Bliss, "Survey of RF Communications and Sensing Convergence Research," in IEEE Access, vol. 5, pp. 252-270, 2017, doi: 10.1109/ACCESS.2016.2639038.
- [2] X. -H. Ding, W. -W. Yang, W. Qin and J. -X. Chen, "A Broadside Shared Aperture Antenna for (3.5, 26) GHz Mobile Terminals With Steerable Beam in Millimeter-Waveband," in IEEE Transactions on Antennas and Propagation, vol. 70, no. 3, pp. 1806-1815, March 2022, doi: 10.1109/TAP.2021.3118817.
- [3] M. Ikram, N. Nguyen-Trong and A. M. Abbosh, "Common-Aperture Sub-6 GHz and Millimeter-Wave 5G Antenna System," in IEEE Access, vol. 8, pp. 199415-199423, 2020, doi: 10.1109/ACCESS.2020.3034887.
- [4] M. Ramzan, A. N. Barreto and P. Sen, "Meta-surface Boosted Antenna to achieve higher than 50 dB TRX Isolation at 26 GHz for Joint Communication and Radar Sensing (JC&S)," 2022 16th European Conference on Antennas and Propagation (EuCAP), 2022, pp. 1-5, doi: 10.23919/EuCAP53622.2022.9769327.
- [5] M. Heino, C. Baquero Barneto, T. Riihonen and M. Valkama, "Design of Phased Array Architectures for Full-Duplex Joint Communications and Sensing," 2021 15th European Conference on Antennas and Propagation (EuCAP), 2021, pp. 1-5, doi: 10.23919/EuCAP51087.2021.9411430.
- [6] R. G. Vaughan and J. B. Andersen, "Antenna diversity in mobile communications," in IEEE Transactions on Vehicular Technology, vol. 36, no. 4, pp. 149-172, Nov. 1987, doi: 10.1109/T-VT.1987.24115.
- [7] G. F. Pedersen, S. Widell and T. Ostervall, "Handheld antenna diversity evaluation in a DCS-1800 small cell," Proceedings of 8th International Symposium on Personal, Indoor and Mobile Radio Communications - PIMRC '97, 1997, pp. 584-588 vol.2, doi: 10.1109/PIMRC.1997.631099.
- [8] A. Razavi, A. A. Glazunov, P. -S. Kildal and J. Yang, "Characterizing Polarization-MIMO Antennas in Random-LOS Propagation Channels," in IEEE Access, vol. 4, pp. 10067-10075, 2016, doi: 10.1109/ACCESS.2016.2637443.